

# Altermagnetism and Strain Induced Altermagnetic Transition in Cairo Pentagonal Monolayer

Shuyi Li,<sup>1</sup> Yu Zhang,<sup>1</sup> Adrian Bahri,<sup>1</sup> Xiaoliang Zhang,<sup>1</sup> and Chunjing Jia<sup>1,\*</sup>

<sup>1</sup>*Department of Physics, University of Florida, Gainesville, FL 32611, USA*

(Dated: December 24, 2024)

Altermagnetism, a recently discovered class of magnetic order characterized by vanishing net magnetization and spin-splitting band structures, has garnered significant research attention. In this work, we introduce a novel two-dimensional system that exhibits  $g$ -wave altermagnetism and undergoes a strain-induced transition from  $g$ -wave to  $d$ -wave altermagnetism. This system can be realized in an unconventional monolayer Cairo pentagonal lattice, for which we present a realistic tight-binding model that incorporates both magnetic and non-magnetic sites. Furthermore, we demonstrate that non-trivial band topology can emerge in this system by breaking the symmetry that protects the spin-polarized nodal points. Finally, *ab initio* calculations on several candidate materials, such as FeS<sub>2</sub> and Nb<sub>2</sub>FeB<sub>2</sub>, which exhibit symmetry consistent with the proposed tight-binding Hamiltonian, are also presented. These findings open new avenues for exploring spintronic devices based on altermagnetic systems.

## INTRODUCTION

Recently, altermagnetism has attracted growing research interest due to its unconventional behavior, which is distinct from traditional collinear ferromagnetism and antiferromagnetism [1–8]. In altermagnet, magnetic moments form an antiferromagnetic-like order with zero net magnetization, while it exhibits energy splitting between states with opposite spins, similar to ferromagnets. A variety of materials have been proposed or confirmed to exhibit altermagnetism through first-principles calculations and experiments, including RuO<sub>2</sub> [9–11], MnTe [12–15], FeSb<sub>2</sub> [16], and CrSb [17]. The unique electronic structure in altermagnets leads to numerous interesting effects and potential applications, such as spin-splitting torque phenomena [18, 19], unconventional superconductivity [20–27], and distinct variants of Hall effect [28–36]. In addition, altermagnets hold great promise for spintronic applications due to their large spin-splitting and robustness against magnetic field perturbations [2, 37, 38].

One of the most fundamental questions in the study of altermagnetic materials is how to understand the origin of this emergent behavior, which is essential for predicting new physical properties and exploring potential applications. At the microscopic level, several mechanisms for the emergence of altermagnetism have been proposed, including the interplay between magnetic and nonmagnetic atoms and the anisotropic ordering of local orbitals [22, 39]. Thus, identifying realistic tight-binding models from a microscopic perspective is crucial for fully understanding this unconventional phenomenon. While several studies have explored altermagnetism using effective models, only a few have investigated the microscopic origin of altermagnetic properties [22, 39–42].

In our work, we investigate the microscopic theory for the origin of altermagnetism on a novel two-dimensional

pentagonal structure [43], known as the Cairo Pentagon. We uncover the mystery of altermagnetism on the Cairo pentagonal lattice at a microscopic level by constructing a simple but realistic tight-binding model containing both magnetic and non-magnetic atoms, and demonstrate that the interplay between them plays a key role in the origin of altermagnetism. Another remarkable feature of the pentagonal lattice is its sensitivity to strain, which induces strong in-plane anisotropy [44–46]. This anisotropy alters the spin-lattice symmetry, thereby impacting the structure of spin-splitting. Calculated band structure using the tight-binding model shows that this strong dependence on strain will lead to a transition between  $g$ -wave and  $d$ -wave altermagnetism. In addition, we find that this pentagonal altermagnet hosts symmetry protected polarized nodal points, and we give examples demonstrating how breaking this symmetry could gap out these nodal points and lead to non-trivial topological bands. Finally, we examine two candidate materials FeS<sub>2</sub> and Nb<sub>2</sub>FeB<sub>2</sub> through *ab initio* calculations, the results successfully reproduce the altermagnetism and its transition under strain as we expect.

Our results represent the first demonstration of strain tuning to achieve different altermagnetic orders in realistic systems, along with a microscopic understanding of the underlying mechanisms. This paves a new avenue for the design and application of strain-tuned spintronic devices based on altermagnetism.

## RESULTS

### Cairo pentagonal lattice structure and model Hamiltonian

We consider a Cairo pentagonal lattice with space group  $P4/mbm$ , shown in Fig. 1a. Due to the presence of non-magnetic sites, the opposite spin sublattices can not be mapped to each other by the combination of time-reversal with translation or inversion, which makes it an ideal platform to investigate the relationship between atomic interplay and altermagnetism.

\* Correspondence e-mail address: chunjing@phys.ufl.edu

The lattice is centrosymmetric due to the four-fold rotation symmetry  $C_{4z}$ . In one primitive unit cell, there are two magnetic atoms with opposite collinear spins and four non-magnetic atoms. The presence of non-magnetic sites breaks time-reversal symmetry while preserving symmetries  $\{C_{2\perp}||\mathcal{M}_x\}$ ,  $\{C_{2\perp}||\mathcal{M}_y\}$ ,  $\{C_{2\perp}||\mathcal{M}_{xy}\}$  and  $\{C_{2\perp}||\mathcal{M}_{\bar{x}y}\}$  relating two magnetic sublattices, where  $C_{2\perp}$  is the  $180^\circ$  rotation operator around an axis perpendicular to the spins,  $\mathcal{M}_x$ ,  $\mathcal{M}_y$ ,  $\mathcal{M}_{xy}$  and  $\mathcal{M}_{\bar{x}y}$  are the mirror operators about the  $x$  axis,  $y$  axis, and the diagonals  $xy$  and  $\bar{x}y$ . Due to symmetry considerations, the pair of electronic states with opposite spins split at general  $k$  points but remain degenerate along  $k_y = 0$ ,  $k_x = 0$ ,  $k_x = k_y$  and  $k_x = -k_y$  in the first Brillouin zone, as shown in Fig. 1c. This unconventional spin-splitting ensures that the magnetic pentagonal crystal is classified as an altermagnet.

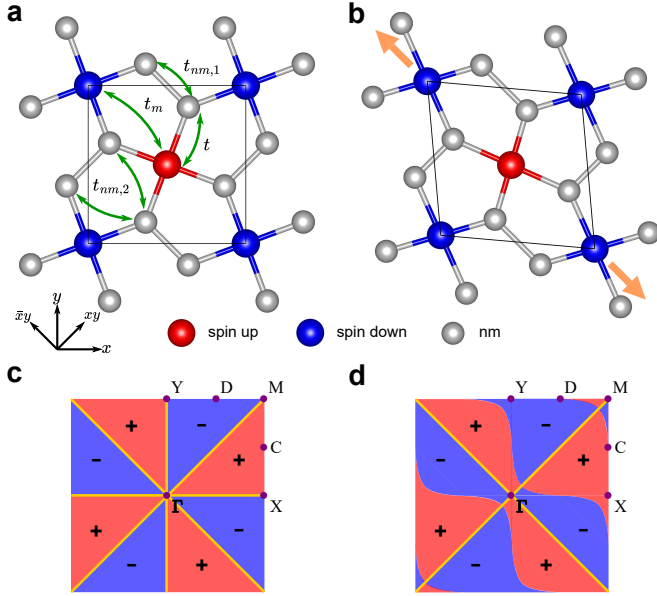


Figure 1. **Cairo pentagonal lattice structure and its electronic energy bands.** **a** A schematics of the pentagonal lattice with space group  $P4/mbm$  and the tight-binding model parameters. The magnetic sites with spin-up, spin-down, and non-magnetic (nm) sites are represented by red, blue, and gray colors.  $t$ ,  $t_m$ ,  $t_{nm,1}$  and  $t_{nm,2}$  represent the hopping strengths between the nearest-neighbor magnetic and non-magnetic sites, the nearest-neighbor magnetic sites, the first nearest-neighbor non-magnetic sites, and the second nearest-neighbor non-magnetic sites, respectively. **b** A schematics of the same pentagonal lattice under diagonal strain along  $xy$  or  $\bar{x}y$ . **c** and **d** Visualization of the higher energy bands from the pair of spin-split bands on this lattice, without and with strain, in the first Brillouin zone. The bands with spin up and down are represented by red and blue, respectively. The yellow lines represent the spin-degenerate nodal lines that cross the  $\Gamma$  point. A number of high-symmetry momentum points are highlighted.

To model the electronic structure in this pentagonal

lattice, we consider a tight-binding Hamiltonian including both magnetic and non-magnetic sites in Eq. (1):

$$H = - \sum_{(i,j),\sigma} t_{ij} c_{i\sigma}^\dagger c_{j\sigma} - J \sum_{i \in m, \sigma, \sigma'} \mathbf{S}_i \cdot c_{i\sigma}^\dagger \boldsymbol{\sigma}_{\sigma\sigma'} c_{i\sigma'} + (\epsilon_m - \mu) \sum_{i \in m, \sigma} c_{i\sigma}^\dagger c_{i\sigma} + (\epsilon_{nm} - \mu) \sum_{i \in nm, \sigma} c_{i\sigma}^\dagger c_{i\sigma}, \quad (1)$$

where  $c_{i\sigma}^{(\dagger)}$  is the annihilation (creation) operator of an electron at site  $i$  with spin  $\sigma = \uparrow, \downarrow$ , and the hopping strength between electrons at sites  $i$  and  $j$  is described by  $t_{ij}$ . In our model, we take into account the hopping  $t$  between the nearest-neighbor magnetic site and non-magnetic site, the hopping  $t_m$  between the nearest-neighbor magnetic sites, and the hopping  $t_{nm,1}$  ( $t_{nm,2}$ ) between the first (second) nearest-neighbor non-magnetic sites.  $J$  is the coupling between the electronic spins and localized magnetic moments  $\mathbf{S}_i$ , and  $\boldsymbol{\sigma}$  is the Pauli matrix. In this work, we set  $\mathbf{S}_i = (0, 0, S e^{i\mathbf{q}\cdot\mathbf{r}_i})$  with magnetic wave vector  $\mathbf{q} = (\pi/a, \pi/a)$  and  $S = 1$ . The on-site energy of magnetic and non-magnetic sites and their chemical potential are denoted by  $\epsilon_m$ ,  $\epsilon_{nm}$  and  $\mu$ .

We obtain the electronic band structure by diagonalizing the Hamiltonian matrix at each momentum point (see details in the supplementary material). Without spin-orbit coupling, there are no interactions between electrons with opposite spins, and thus spin  $\sigma$  is a good quantum number. Finally, the Hamiltonian in Eq. (1) becomes

$$H = \sum_{n, \mathbf{k}, \sigma} E_{n, \sigma}(\mathbf{k}) f_{n, \mathbf{k}, \sigma}^\dagger f_{n, \mathbf{k}, \sigma}, \quad (2)$$

where  $f_{n, \mathbf{k}, \sigma}$  ( $f_{n, \mathbf{k}, \sigma}^\dagger$ ) is a fermionic annihilation (creation) operator and  $E_{n, \sigma}(\mathbf{k})$  represents the corresponding energy dispersion of the  $n$ th band with spin  $\sigma$  ( $n = 1, \dots, 6$ , with energy increasing from low to high). For simplicity, we set  $t$  as the energy unit in the following discussion.

### Altermagnetic band splittings of lattice with $C_{4z}$ symmetry

The band dispersion of the above pentagonal lattice Hamiltonian exhibits  $g$ -wave altermagnetism, as shown in Fig. 2. Fig. 2a shows six pairs of bands with inverse spin-splitting along  $\Gamma$ - $C$  and  $\Gamma$ - $D$ . Fig. 2b and 2c plot the energy spin-splitting  $\Delta E_n(\mathbf{k}) = E_{n, \uparrow}(\mathbf{k}) - E_{n, \downarrow}(\mathbf{k})$  for the 4th and 5th pair of bands. In the first Brillouin zone, there are four spin-degenerate nodal lines,  $k_y = 0$ ,  $k_x = 0$ ,  $k_x = k_y$  and  $k_x = -k_y$ , crossing the  $\Gamma$  point, as expected from the symmetry. Additionally, the spin-splitting  $\Delta E_n(\mathbf{k})$  for isolated pairs of bands near the  $\Gamma$  point is directly proportional to  $k_x k_y (k_x^2 - k_y^2)$  (see details in the supplementary material). All these results illustrate that the tight-binding model successfully realizes  $g$ -wave altermagnetism.

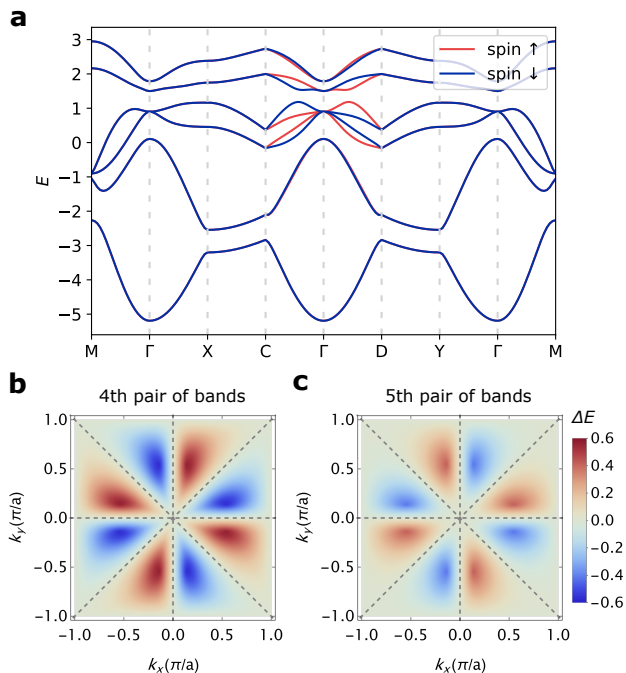


Figure 2. **Band dispersion of pentagonal lattice Hamiltonian with  $C_{4z}$  symmetry.** **a** The electronic band structure along the chosen  $\mathbf{k}$  path in the first Brillouin zone. The parameters used are  $t_m = 0.2$ ,  $t_{nm,1} = 0.9$ ,  $t_{nm,2} = 0.6$ ,  $J = 1$ ,  $\epsilon_m = \epsilon_{nm} = 0$  and  $\mu = 0$ . The spin up and spin down bands are shown in red and blue, respectively. **b** and **c** False color plots of the spin-splitting energy  $\Delta E_n(\mathbf{k}) = E_{n,\uparrow}(\mathbf{k}) - E_{n,\downarrow}(\mathbf{k})$  for the 4th and 5th pair of bands in the first Brillouin zone. Four dashed lines represent the spin-degenerate nodal lines that cross the  $\Gamma$  point.

To understand the origin of  $g$ -wave altermagnetism in this pentagonal lattice, we investigate the dependence of spin-splitting on parameters of the tight-binding Hamiltonian in Eq. (1). The maximal energy splitting of the  $n$ -th pair of bands  $|\Delta E_n|_{max} = \text{Max}[|\Delta E_n(\mathbf{k})|]$  as a function of  $J$ ,  $t_m$ ,  $t_{nm,1}$  and  $t_{nm,2}$  is summarized in Fig. 3. The spin-splitting exhibits a complex dependence on the parameters of the tight-binding model, and the different pairs of electronic bands show significant distinctions. It is evident that the hopping  $t$  between magnetic and non-magnetic sites, and the coupling  $J$  between the electronic spins and localized magnetic moments are necessary for the system to exhibit altermagnetism. If  $t = 0$ , the magnetic sites form a normal Néel antiferromagnet; while if  $J = 0$ , there is no distinction between the sub-Hamiltonians for spin up and down.

In addition to these factors, all energy splittings  $|\Delta E_n|_{max}$  vanish when either  $t_{nm,1}$  or  $t_{nm,2}$  becomes zero. In these cases, the Hamiltonian in Eq. (1) always exhibits band degeneracy  $E_{n,\sigma}(k_x, k_y) = E_{n,\sigma}(k_x, -k_y) = E_{n,\sigma}(-k_x, k_y)$ , as well as symmetries  $\{C_{2\perp}||\mathcal{M}_x\}$  and  $\{C_{2\perp}||\mathcal{M}_y\}$  (see details in the sup-

plementary material), which lead to band degeneracy  $E_{n,\uparrow}(\mathbf{k}) = E_{n,\downarrow}(\mathbf{k})$  at all  $\mathbf{k}$  points. The above reasoning indicates that the hopping terms between non-magnetic sites are also crucial for the emergence of altermagnetic spin splitting in the pentagonal lattice.

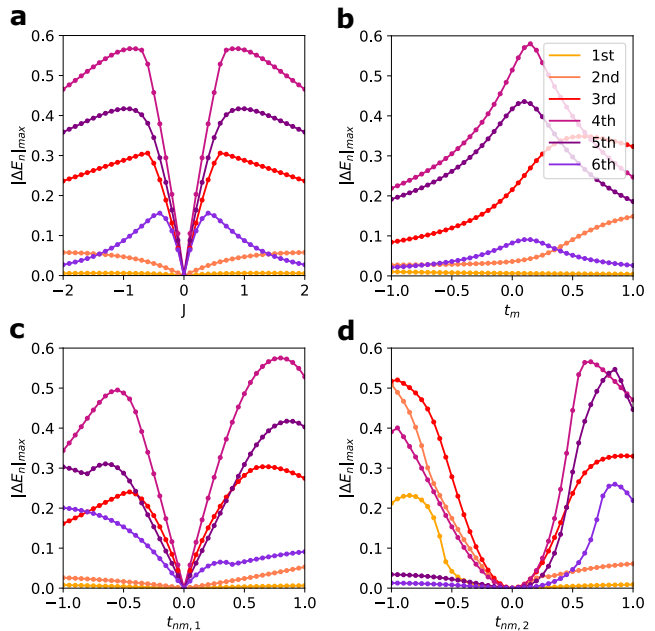


Figure 3. **Dependence of spin-splitting energy on tight-binding model parameters.** Plots of the maximal energy splitting for the  $n$ -th pair of bands,  $|\Delta E_n|_{max}$ , as a function of **a**  $J$ , **b**  $t_m$ , **c**  $t_{nm,1}$ , and **d**  $t_{nm,2}$ , while other parameters are fixed as  $t_m = 0.2$ ,  $t_{nm,1} = 0.9$ ,  $t_{nm,2} = 0.6$ ,  $J = 1$ ,  $\epsilon_m = \epsilon_{nm} = 0$  and  $\mu = 0$ . Different colors represent the band pairs, ordered from lower to higher energy.

### Altermagnetic band splittings of lattice under $xy$ and $\bar{x}y$ strains

Next, we study the impact of strain along the diagonal directions  $xy$  and  $\bar{x}y$  on the altermagnetism of the Cairo pentagonal lattice, as shown in Fig. 1b. After applying the strain, a significant in-plane anisotropy emerges due to the lattice's sensitivity to it. This anisotropy breaks the lattice symmetry  $C_{4z}$ , and the symmetries  $\{C_{2\perp}||\mathcal{M}_x\}$  and  $\{C_{2\perp}||\mathcal{M}_y\}$  relating two magnetic sublattices, while preserving two other symmetries  $\{C_{2\perp}||\mathcal{M}_{xy}\}$  and  $\{C_{2\perp}||\mathcal{M}_{\bar{x}y}\}$ . The change in symmetry results in a transformation in the structure of unconventional spin-splitting, as shown in Fig. 1d.

To incorporate the effect of strain into the tight-binding Hamiltonian, we introduce anisotropic hopping between sites along the  $xy$  and  $\bar{x}y$  directions. Consequently, the hopping term in Eq. (1) is modified as

$$H_S^{hp} = -(1 + \delta) \sum_{\langle i,j \rangle_{xy}} t_{ij} c_{i\sigma}^\dagger c_{j\sigma} - (1 - \delta) \sum_{\langle i,j \rangle_{\bar{x}y}} t_{ij} c_{i\sigma}^\dagger c_{j\sigma}, \quad (3)$$

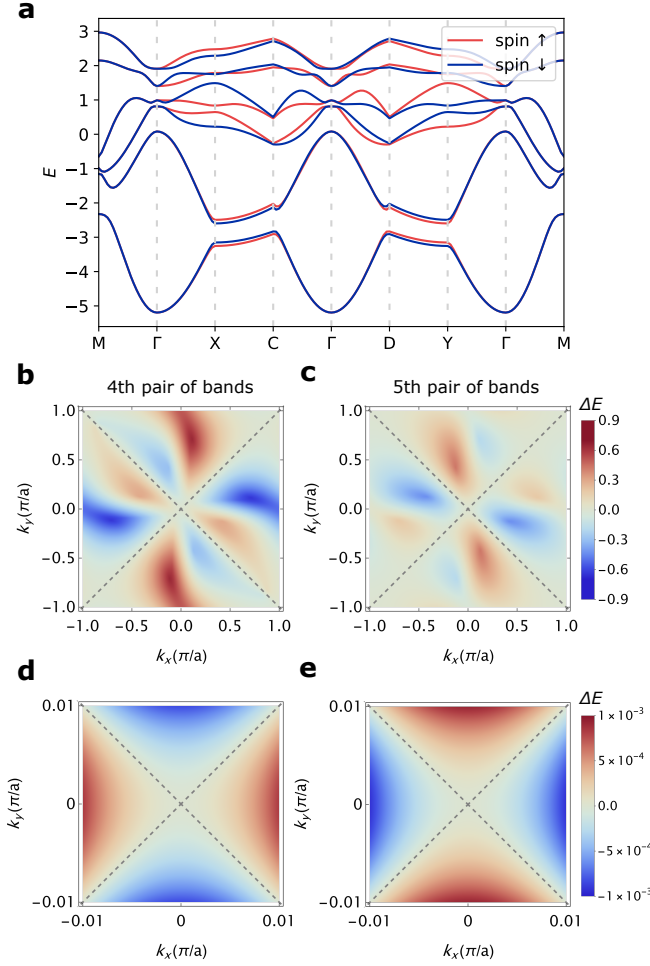


Figure 4. **Band dispersion of pentagonal lattice Hamiltonian under  $xy$  and  $\bar{xy}$  strains.** **a** The electronic band structure along the chosen  $\mathbf{k}$  path in the first Brillouin zone. The parameters used are  $\delta = 0.1$ ,  $t_m = 0.2$ ,  $t_{nm,1} = 0.9$ ,  $t_{nm,2} = 0.6$ ,  $J = 1$ ,  $\epsilon_m = \epsilon_{nm} = 0$  and  $\mu = 0$ . The bands of spin up and down are labeled by red and blue. **b** and **c** False color plots of the spin-splitting energy  $\Delta E_n(\mathbf{k}) = E_{n,\uparrow}(\mathbf{k}) - E_{n,\downarrow}(\mathbf{k})$  for the 4th and 5th pair of bands in the first Brillouin zone. **d** and **e** Plots of  $\Delta E_n(\mathbf{k})$  near the  $\Gamma$  points, within  $|k_x| \leq 10^{-2}\pi/a$  and  $|k_y| \leq 10^{-2}\pi/a$ .

where the anisotropy  $\delta$  reflects the strength of strain.

The band dispersion relations are shown in Fig. 4a. Unlike the previous case, six pairs of bands now exhibit inverse spin splitting along  $X-\Gamma-C$  and  $Y-\Gamma-D$ . The energy spin-splittings  $\Delta E_n(\mathbf{k})$  shown in Fig. 4b and Fig. 4c demonstrate that there are only two spin-degenerate nodal lines,  $kx = \pm ky$ , crossing the  $\Gamma$  point, while the two former nodal lines are shifted away. The change in nodal lines is consistent with the symmetry breaking induced by diagonal strain, while the two preserved symmetries  $\{C_{2\perp}||\mathcal{M}_{xy}\}$  and  $\{C_{2\perp}||\mathcal{M}_{\bar{xy}}\}$  enforce the existence of the remaining two nodal lines. In Fig. 4d and Fig. 4e, we zoom in on the above plots near the  $\Gamma$  point, where the

spin-splitting  $\Delta E_n(\mathbf{k})$  is directly proportional to  $k_x^2 - k_y^2$  (see details in the supplementary material) and thus exhibits  $d$ -wave symmetry. Consequently, as a result of the applied strain, the system transitions from a  $g$ -wave to a  $d$ -wave altermagnetism in the neighborhood of the  $\Gamma$  point.

Additionally, we examine the dependence of spin-splitting on the strain strength. Fig. 5a illustrates the maximal spin-splitting  $|\Delta E_n|_{max}$  as a function of anisotropy  $\delta$ . The sensitivity of the band splitting to strain varies among different pairs of bands. Within the range of  $|\delta| \leq 0.5$ , the maximum splitting can reach slightly higher than the energy level of  $t$ . For comparison, Fig. 5b depicts the case where the next-nearest-neighbor hopping between the magnetic and nonmagnetic sites  $t_{nm,2}$  is zero. As discussed earlier, the unstrained system exhibits normal spin-degeneracy in this case. Upon applying diagonal strain, the system transitions from a normal antiferromagnetic phase to a  $d$ -wave altermagnetic phase, with the maximal spin-splitting showing an almost linear dependence on  $\delta$  for small values of  $\delta$ .

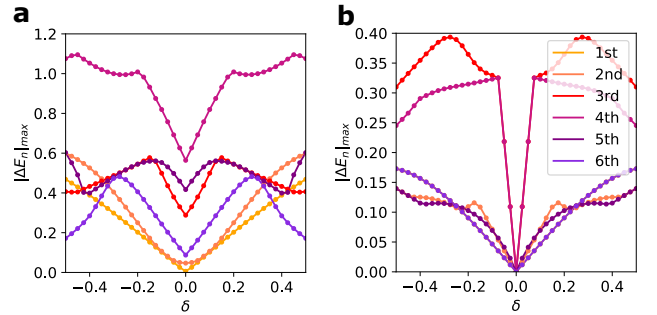


Figure 5. **Dependence of spin-splitting on strain strength.** Plots of the maximal energy splitting for the  $n$ -th pair of bands,  $|\Delta E_n|_{max}$ , as a function of anisotropy  $\delta$  under **a**  $t_{nm,2} = 0.6$  and **b**  $t_{nm,2} = 0$ , with other parameters being  $t_m = 0.2$ ,  $t_{nm,1} = 0.9$ ,  $t_{nm,2} = 0.6$ ,  $J = 1$ ,  $\epsilon_m = \epsilon_{nm} = 0$  and  $\mu = 0$ . Different colors represent the band pairs, ordered from lower to higher energy.

## Polarized Nodal Points and Band Topology

In addition to the nodal lines formed by spin-degeneracy, several spin-polarized nodal points are present in this altermagnetic pentagonal lattice. As shown in Fig. 6a, eight spin-polarized nodal points emerge at the band crossings of the 4th and 5th bands with the same spin. These nodal points are protected by the symmetry  $\{\mathcal{T}C_{2\perp}||\mathcal{T}C_{2z}\}$ , with each nodal point carrying a  $\pi$  Berry phase, where  $\mathcal{T}$  represents the time-reversal operator. Thus, nontrivial band topology can be achieved by breaking this symmetry. Here, we explore two mechanisms that gap out the spin-polarized nodal points using toy models: breaking the lattice inversion symmetry  $\{E||C_{2z}\}$  through the anisotropic hopping

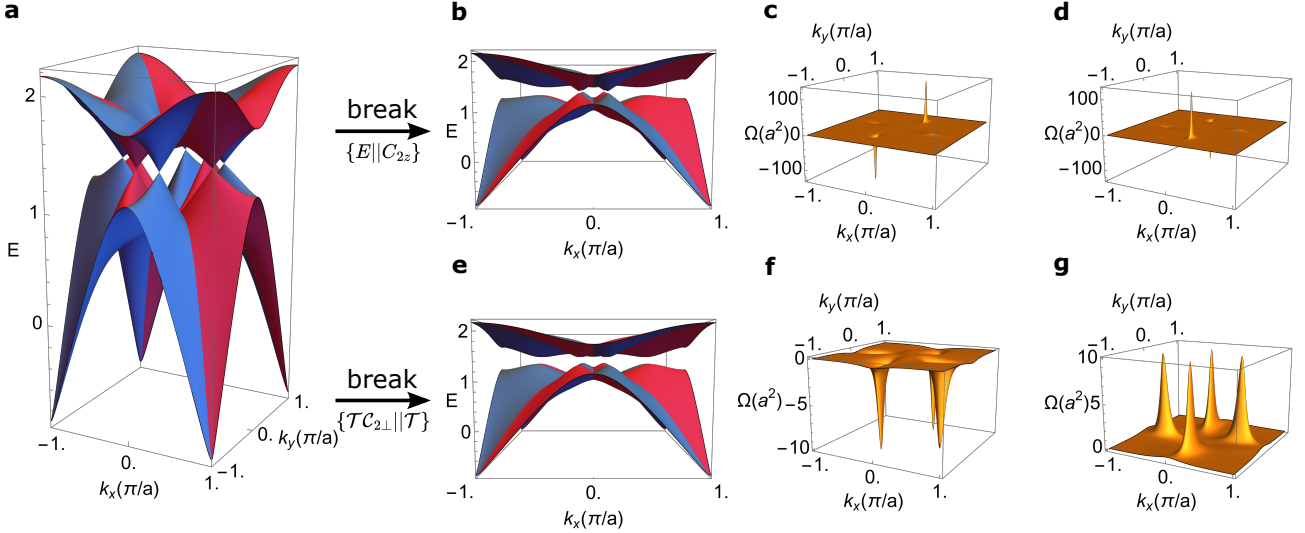


Figure 6. **Band structure and Berry curvature after gapping out the polarized nodal points.** **a** Eight spin polarized nodal points formed by band crossing between the 4th and 5th pairs of bands. **b** The electronic band structure for the 4th and 5th pairs of bands under inversion symmetry  $\{E||C_{2z}\}$  breaking with  $t_1 = 0.2$ , and **c**, **d** the corresponding Berry curvature  $\Omega(\mathbf{k})$  of the 5th pair of spin-up and spin-down bands. **e** The electronic band structure for the 4th and 5th pairs of bands under inversion symmetry  $\{\mathcal{T}C_{2\perp}||\mathcal{T}\}$  breaking with  $t_2 = 0.2$ , and **f**, **g** the corresponding Berry curvature  $\Omega(\mathbf{k})$  of the 5th pair of spin-up and spin-down bands. The other parameters in the calculations are  $t_m = 0.2$ ,  $t_{nm,1} = 0.9$ ,  $t_{nm,2} = 0.6$ ,  $J = 1$ ,  $\epsilon_m = \epsilon_{nm} = 0$  and  $\mu = 0$ .

term between magnetic atoms, represented by

$$H_1 = \sum_{i \in (m\uparrow), \sigma} \sum_{\xi} (t_1 c_{i,\sigma}^\dagger c_{i+\xi\sigma} - t_1 c_{i\sigma}^\dagger c_{i-\xi,\sigma}) + h.c., \quad (4)$$

and breaking the lattice time-reversal symmetry  $\{\mathcal{T}C_{2\perp}||\mathcal{T}\}$  through the complex hopping term between magnetic atoms, represented by

$$H_2 = - \sum_{i \in (m\uparrow), \sigma} (-1)^\sigma \sum_{\xi} i(t_2 c_{i,\sigma}^\dagger c_{i+\xi\sigma} + t_2 c_{i\sigma}^\dagger c_{i-\xi,\sigma}) + h.c., \quad (5)$$

where  $\xi = \frac{1}{2}a\hat{x} \pm \frac{1}{2}a\hat{y}$ .

The impact of breaking the symmetry  $\{E||C_{2z}\}$  using Eq. (4) is illustrated in Fig. 6b. All spin-polarized nodal points are gapped out, while the spin-degeneracy nodal lines are preserved. We plot the Berry curvature  $\Omega(\mathbf{k})$  of the 5th pairs of bands with opposite spins after inversion symmetry breaking in Fig. 6c and Fig. 6d, where the peaks of  $\Omega(\mathbf{k})$  appear at the former nodal points. In this case, the Berry curvature satisfies  $\Omega(\mathbf{k}) = -\Omega(-\mathbf{k})$  for all  $\mathbf{k}$  points, resulting in Chern number  $\mathcal{C}_\sigma = 0$ . In contrast, the band structure after  $\{\mathcal{T}C_{2\perp}||\mathcal{T}\}$  symmetry breaking using Eq. (5) and the Berry curvature of the 5th pairs of bands are shown in Fig. 6e, Fig. 6f and Fig. 6g. In each band, this symmetry-breaking term in Eq. (5) leads to an equivalent contribution from four nodal points. This mechanism mirrors the behavior seen in Haldane's model, making the 5th pair of bands topologically non-trivial with a Chern number  $\mathcal{C}_\sigma = \mp 2$ .

## Candidate Materials

A two-dimensional form of pyrite,  $\text{FeS}_2$ , has been predicted to exhibit a Cairo pentagonal structure with antiferromagnetic order [47]. It belongs to space group  $P4/mbm$  (No.127) and point group  $D_{4h}$ . Fig. 7a shows the crystal structure, where each Fe atom is surrounded by four S atoms. To examine the magnetic ground state, we perform *ab initio* calculations to calculate the energy of different collinear magnetic states on this planar structure under geometry optimizations (see details in the supplementary material). The result indicates that the most stable configuration exhibits the Néel antiferromagnetic order on Fe atoms while S atoms are non-magnetic, as shown in Fig. 7a.

Thus, this planar  $\text{FeS}_2$  structure corresponds to the pentagonal lattice system discussed above. In particular, it exhibits the symmetries  $\{C_{2\perp}||\mathcal{M}_x\}$ ,  $\{C_{2\perp}||\mathcal{M}_y\}$ ,  $\{C_{2\perp}||\mathcal{M}_{xy}\}$ , and  $\{C_{2\perp}||\mathcal{M}_{\bar{xy}}\}$ , which relate two magnetic sublattices. The electronic band structure obtained from *ab initio* calculations is shown in Fig. 7b, displaying features consistent with the tight-binding model result in Fig. 2a, that inverse spin-splitting occurs along the  $\Gamma$ - $C$  and  $\Gamma$ - $D$  paths, while spin-degeneracy is observed along the  $\Gamma$ - $X$ ,  $\Gamma$ - $Y$ , and  $\Gamma$ - $M$  paths. These behaviors characterize planar pentagonal  $\text{FeS}_2$  as a *g*-wave altermagnet as expected. Additionally, we present the spin density iso-surfaces for bands with different levels of spin-splitting in Fig. 7c and Fig. 7d, where a larger spin-splitting coincides with a more anisotropic spin density.

Next, we study the effect of strains along the diago-

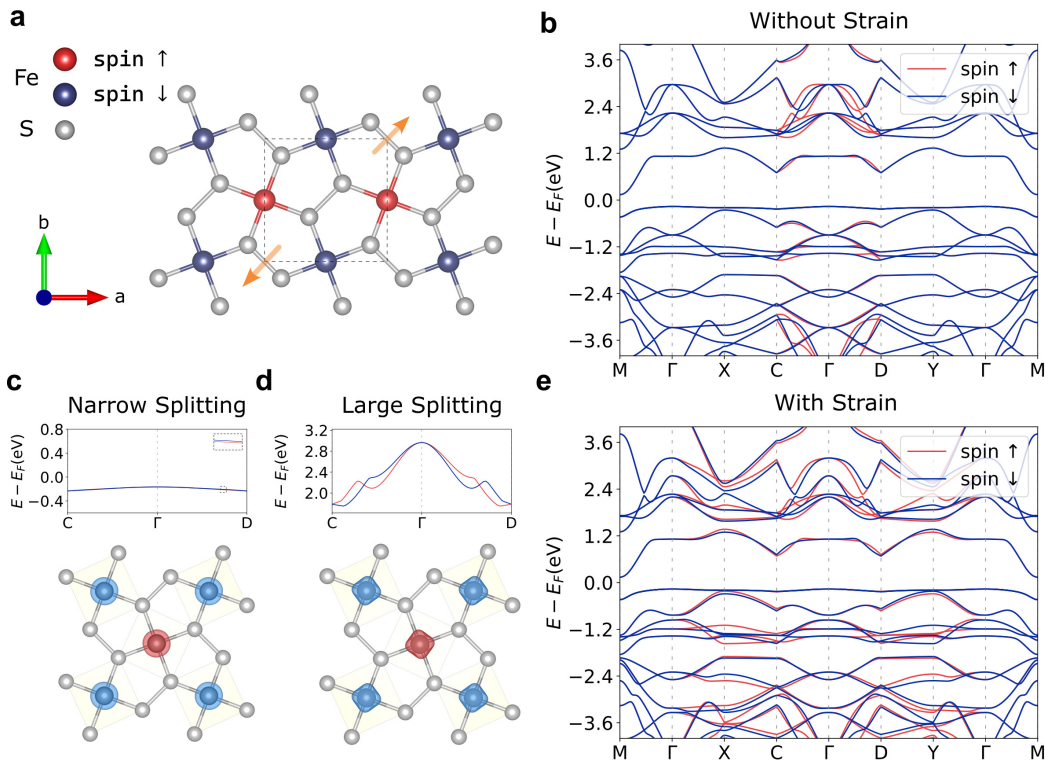


Figure 7. **Crystal structure and electronic bands of FeS<sub>2</sub>.** **a** Crystal structure of FeS<sub>2</sub>. The red and blue colors of Fe atoms indicate the directions of their localized magnetic moments, while the orange arrows represent the direction of diagonal strain. **b** The electronic band structure of FeS<sub>2</sub> without strain. **c** and **d** Spin density isosurfaces for two pairs of bands without strain, illustrating narrow and large spin-splitting, respectively (the inset zooms in on energy by a factor of 5). **e** The electronic band structure of FeS<sub>2</sub> with diagonal strain, where the angle  $\gamma$  between lattice parameters  $a$  and  $b$  is tuned to  $\gamma = 88^\circ$ .

nal directions on planar FeS<sub>2</sub>, as indicated by the arrows in Fig. 7a. We introduce the strain in *ab initio* calculations by slightly reducing the angle  $\gamma$  between lattice vectors  $\mathbf{a}$  and  $\mathbf{b}$  to less than  $90^\circ$ . Fig. 7e presents the electronic band structure for  $\gamma = 88.0^\circ$ , where inverse spin-splitting appears along the  $\Gamma$ -X-C- $\Gamma$  and  $\Gamma$ -Y-D- $\Gamma$  paths, while the bands remain degenerate along the  $\Gamma$ -M path, displaying the same features as in the model result shown in Fig. 4a. This behavior indicates a transition from *g*-wave to *d*-wave altermagnetism, as predicted by the tight-binding model analysis.

In addition to the two-dimensional cases, we highlight Nb<sub>2</sub>FeB<sub>2</sub>, a three-dimensional material predicted to exhibit *g*-wave altermagnetism [48, 49]. Fig. 8a shows the crystal structure of Nb<sub>2</sub>FeB<sub>2</sub>, which consists of alternate layers of Fe-B and Nb atoms along  $c$  axis. Each Fe-B layer exhibits the same Cairo pentagonal structure discussed earlier, and the magnetic Fe atoms carry an in-plane Néel antiferromagnetic spin arrangement. Thus, the previous analysis of symmetry-induced altermagnetism also applies to Nb<sub>2</sub>FeB<sub>2</sub>. Its electronic band structures without and with diagonal strain are shown in Fig. 8c and Fig. 8d, where the angle  $\gamma$  between lattice vectors  $\mathbf{a}$  and  $\mathbf{b}$  is  $90^\circ$  and  $88^\circ$  respectively. These results demonstrate that Nb<sub>2</sub>FeB<sub>2</sub> is a *g*-wave

altermagnet and it undergoes a transition from *g*-wave to *d*-wave altermagnetism under diagonal strain, as expected. Furthermore, in both altermagnetic materials, the spin-splitting increases significantly after applying strain, consistent with the model analysis.

## Conclusion and Discussion

Our study uncovers the first microscopic mechanism underlying *g*-wave altermagnetism in two dimension, realized in Cairo pentagonal lattice. Based on the symmetry analysis, we propose a simple but realistic tight-binding model containing both magnetic and non-magnetic sites that successfully realizes the altermagnetic band spin-splitting with *g*-wave symmetry. The lattice-spin symmetry ensured by the presence of non-magnetic atoms guarantees the existence of altermagnetism in this antiferromagnetically ordered pentagonal system. Our analysis of the dependence of spin-splitting on parameters in the tight-binding model provides one of the mechanisms, that both the hopping between magnetic site and non-magnetic site, and the hopping between non-magnetic sites are indispensable for the altermagnetic behavior. We note that there are other possible origins of altermagnetism, such as the anisotropic ordering of local

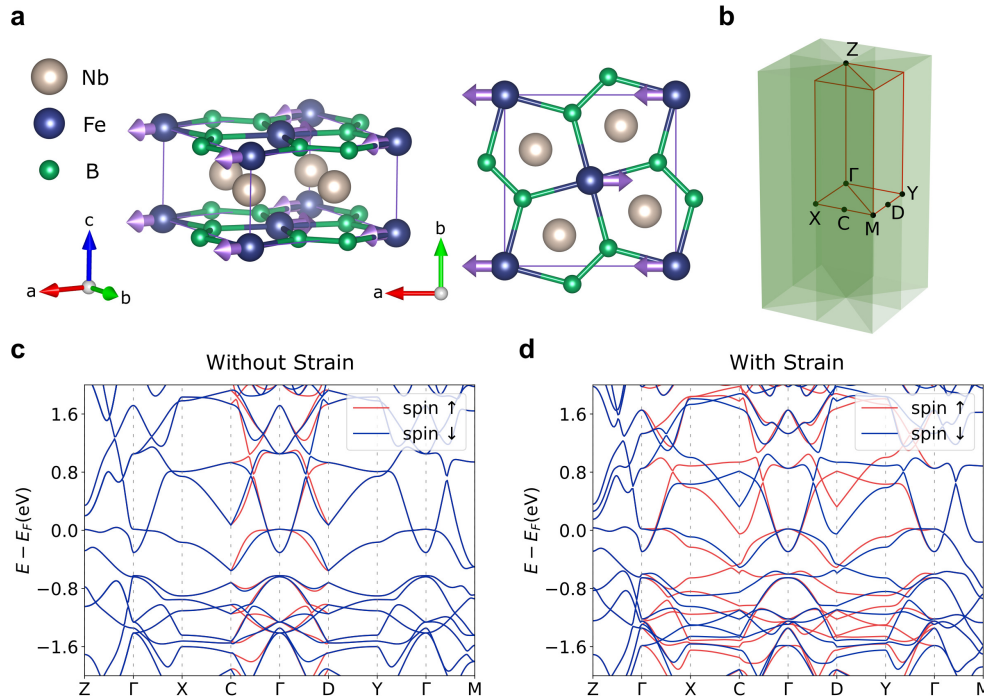


Figure 8. **Crystal structure and electronic bands of  $\text{Nb}_2\text{FeB}_2$ .** **a** Crystal structure of  $\text{Nb}_2\text{FeB}_2$  shown from two perspectives. The purple arrows indicate the directions of localized magnetic moments on Fe atoms. **b** The first Brillouin zone of  $\text{Nb}_2\text{FeB}_2$  and high symmetry moment points of our interest. **c** and **d** The electronic band structures of  $\text{Nb}_2\text{FeB}_2$  under two conditions: without diagonal strain (where the angle  $\gamma$  between lattice parameters  $a$  and  $b$  is  $90^\circ$ ) and with diagonal strain (where  $\gamma = 88^\circ$ ).

orbitals, which are beyond our discussion in this work.

Another important finding from our model is that applying strain to the crystal can induce a transformation in the type of altermagnetism. Strain reduces the original lattice-spin symmetry, introducing anisotropic hopping terms in the tight-binding model and making the spin-splitting behavior more complex. Near the  $\Gamma$  point, we observe that strain applied along the diagonal direction of this pentagonal structure causes a transition from  $g$ -wave to  $d$ -wave altermagnetism. Additionally, we find that this pentagonal altermagnet contains spin-polarized nodal points protected by  $\{\mathcal{T}C_{2\perp} || \mathcal{T}C_{2z}\}$  symmetry. Breaking this symmetry could lead to non-trivial topological bands and the quantum Hall effect for electrons.

Finally, we identify several candidate materials through *ab initio* calculations, including monolayer  $\text{FeS}_2$  and bulk  $\text{Nb}_2\text{FeB}_2$ , which show promise for exploring altermagnetism in Cairo pentagonal crystal structures. In particular, we examine the effect of diagonal strain on these crystals, observing that altermagnetism transforms from  $g$ -wave to  $d$ -wave as expected. These findings sug-

gest new paradigm of tuning the type of altermagnetism by strain, opening new possibilities for enabling strain-tuned spintronic devices and the interplay with other degrees of freedom.

## METHODS

We use Vienna Ab initio Simulation Package (VASP) [50] for all density functional theory calculations. Projector-augmented-wave (PAW) potential was utilized for ion-electron interaction, and the generalized gradient approximation (GGA) with the Perdew-Burke-Ernzerhof (PBE) functional [51] was applied to describe electron exchange-correlation interaction. The energy cutoff was set to be 600 eV. More details are in the supplementary material.

## CODE AVAILABILITY

The codes and scripts used for the numerical calculations reported in this paper are available from the first author (S.L.) upon request.

## DATA AVAILABILITY

The data analyzed in the present study is available from the first author (S.L.) upon request.

[1] L. Šmejkal, J. Sinova, and T. Jungwirth, Beyond conventional ferromagnetism and antiferromagnetism: A phase

with nonrelativistic spin and crystal rotation symmetry,

- Physical Review X **12**, 031042 (2022).
- [2] L. Šmejkal, J. Sinova, and T. Jungwirth, Emerging research landscape of altermagnetism, Physical Review X **12**, 040501 (2022).
  - [3] L. Šmejkal, A. H. MacDonald, J. Sinova, S. Nakatsuji, and T. Jungwirth, Anomalous hall antiferromagnets, Nature Reviews Materials **7**, 482 (2022).
  - [4] S. Hayami, Y. Yanagi, and H. Kusunose, Bottom-up design of spin-split and reshaped electronic band structures in antiferromagnets without spin-orbit coupling: Procedure on the basis of augmented multipoles, Physical Review B **102**, 144441 (2020).
  - [5] S. Hayami, Y. Yanagi, and H. Kusunose, Momentum-dependent spin splitting by collinear antiferromagnetic ordering, journal of the physical society of japan **88**, 123702 (2019).
  - [6] R. González-Hernández, L. Šmejkal, K. Výborný, Y. Yahagi, J. Sinova, T. c. v. Jungwirth, and J. Železný, Efficient electrical spin splitter based on nonrelativistic collinear antiferromagnetism, Phys. Rev. Lett. **126**, 127701 (2021).
  - [7] L.-D. Yuan, Z. Wang, J.-W. Luo, E. I. Rashba, and A. Zunger, Giant momentum-dependent spin splitting in centrosymmetric low-z antiferromagnets, Physical Review B **102**, 014422 (2020).
  - [8] L.-D. Yuan, Z. Wang, J.-W. Luo, and A. Zunger, Prediction of low-z collinear and noncollinear antiferromagnetic compounds having momentum-dependent spin splitting even without spin-orbit coupling, Physical Review Materials **5**, 014409 (2021).
  - [9] Z. Feng, X. Zhou, L. Šmejkal, L. Wu, Z. Zhu, H. Guo, R. González-Hernández, X. Wang, H. Yan, P. Qin, *et al.*, An anomalous hall effect in altermagnetic ruthenium dioxide, Nature Electronics **5**, 735 (2022).
  - [10] O. Fedchenko, J. Minár, A. Akashdeep, S. W. D'Souza, D. Vasilyev, O. Tkach, L. Odenbreit, Q. Nguyen, D. Kutnyakhov, N. Wind, *et al.*, Observation of time-reversal symmetry breaking in the band structure of altermagnetic ruo2, Science advances **10**, eadj4883 (2024).
  - [11] X. Zhou, W. Feng, R. Zhang, L. Šmejkal, J. Sinova, Y. Mokrousov, and Y. Yao, Crystal thermal transport in altermagnetic ruo2 (2023), arXiv preprint arXiv:2305.01410.
  - [12] S. Lee, S. Lee, S. Jung, J. Jung, D. Kim, Y. Lee, B. Seok, J. Kim, B. G. Park, L. Šmejkal, *et al.*, Broken kramers degeneracy in altermagnetic mnte, Physical Review Letters **132**, 036702 (2024).
  - [13] T. Osumi, S. Souma, T. Aoyama, K. Yamauchi, A. Honma, K. Nakayama, T. Takahashi, K. Ohgushi, and T. Sato, Observation of a giant band splitting in altermagnetic mnte, Physical Review B **109**, 115102 (2024).
  - [14] J. Krempaský, L. Šmejkal, S. D'souza, M. Hajlaoui, G. Springholz, K. Uhlířová, F. Alarab, P. Constantinou, V. Strocov, D. Usanov, *et al.*, Altermagnetic lifting of kramers spin degeneracy, Nature **626**, 517 (2024).
  - [15] Z. Liu, M. Ozeki, S. Asai, S. Itoh, and T. Masuda, Chiral split magnon in altermagnetic mnte, Physical Review Letters **133**, 156702 (2024).
  - [16] I. I. Mazin, K. Koepernik, M. D. Johannes, R. González-Hernández, and L. Šmejkal, Prediction of unconventional magnetism in doped fesb2, Proceedings of the National Academy of Sciences **118**, e2108924118 (2021).
  - [17] I. I. Mazin, K. Koepernik, M. D. Johannes, R. González-Hernández, and L. Šmejkal, Prediction of unconventional magnetism in doped fesb2, Proceedings of the National Academy of Sciences **118**, e2108924118 (2021).
  - [18] H. Bai, L. Han, X. Feng, Y. Zhou, R. Su, Q. Wang, L. Liao, W. Zhu, X. Chen, F. Pan, *et al.*, Observation of spin splitting torque in a collinear antiferromagnet ruo 2, Physical Review Letters **128**, 197202 (2022).
  - [19] S. Karube, T. Tanaka, D. Sugawara, N. Kadoguchi, M. Kohda, and J. Nitta, Observation of spin-splitter torque in collinear antiferromagnetic ruo 2, Physical review letters **129**, 137201 (2022).
  - [20] S. Sumita, M. Naka, and H. Seo, Fulde-ferrell-larkin-ovchinnikov state induced by antiferromagnetic order in  $\kappa$ -type organic conductors, Physical Review Research **5**, 043171 (2023).
  - [21] D. Zhu, Z.-Y. Zhuang, Z. Wu, and Z. Yan, Topological superconductivity in two-dimensional altermagnetic metals, Physical Review B **108**, 184505 (2023).
  - [22] B. Brekke, A. Brataas, and A. Sudbø, Two-dimensional altermagnets: Superconductivity in a minimal microscopic model, Physical Review B **108**, 224421 (2023).
  - [23] S.-B. Zhang, L.-H. Hu, and T. Neupert, Finite-momentum cooper pairing in proximitized altermagnets, Nature Communications **15**, 1801 (2024).
  - [24] D. Chakraborty and A. M. Black-Schaffer, Zero-field finite-momentum and field-induced superconductivity in altermagnets, Physical Review B **110**, L060508 (2024).
  - [25] M. Wei, L. Xiang, F. Xu, L. Zhang, G. Tang, and J. Wang, Gapless superconducting state and mirage gap in altermagnets, Physical Review B **109**, L201404 (2024).
  - [26] K. Mæland, B. Brekke, and A. Sudbø, Many-body effects on superconductivity mediated by double-magnon processes in altermagnets, Physical Review B **109**, 134515 (2024).
  - [27] S. Chourasia, A. Svetogorov, A. Kamra, and W. Belzig, Thermodynamic properties of a superconductor interfaced with an altermagnet, arXiv preprint arXiv:2403.10456 (2024).
  - [28] M. Leiviskä, J. Rial, A. Bad'ura, R. L. Seeger, I. Kounta, S. Beckert, D. Kriegner, I. Joumard, E. Schmoranzarová, J. Sinova, *et al.*, Anisotropy of the anomalous hall effect in thin films of the altermagnet candidate mn 5 si 3, Physical Review B **109**, 224430 (2024).
  - [29] T. Sato, S. Haddad, I. C. Fulga, F. F. Assaad, and J. van den Brink, Altermagnetic anomalous hall effect emerging from electronic correlations, Physical Review Letters **133**, 086503 (2024).
  - [30] L. Attias, A. Levchenko, and M. Khodas, Intrinsic anomalous hall effect in altermagnets, Physical Review B **110**, 094425 (2024).
  - [31] C.-T. Liao, Y.-C. Wang, Y.-C. Tien, S.-Y. Huang, and D. Qu, Separation of inverse altermagnetic spin-splitting effect from inverse spin hall effect in ruo 2, Physical Review Letters **133**, 056701 (2024).
  - [32] H. Jin, Z. Tan, Z. Gong, and J. Wang, Anomalous hall effect in two-dimensional vanadium tetrahalogen with altermagnetic phase, Physical Review B **110**, 155125 (2024).
  - [33] Y. Fang, J. Cano, and S. A. A. Ghorashi, Quantum geometry induced nonlinear transport in altermagnets, Physical Review Letters **133**, 106701 (2024).
  - [34] P. Rao, A. Mook, and J. Knolle, Tunable band topology and optical conductivity in altermagnets, Physical Review B **110**, 024425 (2024).
  - [35] K. Parshukov, R. Wiedmann, and A. P. Schnyder, Topo-



- logical responses from gapped weyl points in 2d altermagnets, arXiv preprint arXiv:2403.09520 (2024).
- [36] C.-Y. Tan, Z.-F. Gao, H.-C. Yang, K. Liu, P.-J. Guo, and Z.-Y. Lu, Bipolarized weyl semimetals and quantum crystal valley hall effect in two-dimensional altermagnetic materials, arXiv preprint arXiv:2406.16603 (2024).
- [37] L. Bai, W. Feng, S. Liu, L. Šmejkal, Y. Mokrousov, and Y. Yao, Altermagnetism: Exploring new frontiers in magnetism and spintronics, *Advanced Functional Materials*, 2409327 (2024).
- [38] L. Šmejkal, A. B. Hellenes, R. González-Hernández, J. Sinova, and T. Jungwirth, Giant and tunneling magnetoresistance in unconventional collinear antiferromagnets with nonrelativistic spin-momentum coupling, *Physical Review X* **12**, 011028 (2022).
- [39] V. Leeb, A. Mook, L. Šmejkal, and J. Knolle, Spontaneous formation of altermagnetism from orbital ordering, *Physical Review Letters* **132**, 236701 (2024).
- [40] M. Roig, A. Kreisel, Y. Yu, B. M. Andersen, and D. F. Agterberg, Minimal models for altermagnetism, *Physical Review B* **110**, 144412 (2024).
- [41] P. Das, V. Leeb, J. Knolle, and M. Knap, Realizing altermagnetism in fermi-hubbard models with ultracold atoms, *Physical Review Letters* **132**, 263402 (2024).
- [42] Y. Sato, S. Haddad, I. C. Fulga, F. F. Assaad, and J. van den Brink, Altermagnetic anomalous hall effect emerging from electronic correlations, *Physical Review Letters* **133**, 086503 (2024).
- [43] Y. Shen and Q. Wang, Pentagon-based 2d materials: Classification, properties and applications, *Physics Reports* **964**, 1 (2022).
- [44] Y. Wang, Y. Li, and Z. Chen, Not your familiar two dimensional transition metal disulfide: structural and electronic properties of the pds 2 monolayer, *Journal of Materials Chemistry C* **3**, 9603 (2015).
- [45] X. Shao, X. Liu, X. Zhao, J. Wang, X. Zhang, and M. Zhao, Electronic properties of a  $\pi$ -conjugated cairo pentagonal lattice: Direct band gap, ultrahigh carrier mobility, and slanted dirac cones, *Physical Review B* **98**, 085437 (2018).
- [46] P. Li, J. Zhang, C. Zhu, W. Shen, C. Hu, W. Fu, L. Yan, L. Zhou, L. Zheng, H. Lei, *et al.*, Penta-pdpse: a new 2d pentagonal material with highly in-plane optical, electronic, and optoelectronic anisotropy, *Advanced Materials* **33**, 2102541 (2021).
- [47] S. Wei, S. Zheng, X. Wen, C. Xie, and J. Liang, A novel antiferromagnetic semiconductor hidden in pyrite, *Computational Materials Science* **183**, 109852 (2020).
- [48] X.-Y. Hou, H.-C. Yang, Z.-X. Liu, P.-J. Guo, and Z.-Y. Lu, Large intrinsic anomalous hall effect in both nb<sub>2</sub>feb<sub>2</sub> and ta<sub>2</sub>feb<sub>2</sub> with collinear antiferromagnetism, *Phys. Rev. B* **107**, L161109 (2023).
- [49] Z.-F. Gao, S. Qu, B. Zeng, Y. Liu, J.-R. Wen, H. Sun, P.-J. Guo, and Z.-Y. Lu, Ai-accelerated discovery of altermagnetic materials, arXiv preprint arXiv:2311.04418 (2023).
- [50] G. Kresse and J. Hafner, Ab initio molecular-dynamics simulation of the liquid-metal-amorphous-semiconductor transition in germanium, *Phys. Rev. B* **49**, 14251 (1994).
- [51] J. P. Perdew, K. Burke, and M. Ernzerhof, Generalized gradient approximation made simple, *Phys. Rev. Lett.* **77**, 3865 (1996).

## ACKNOWLEDGEMENTS

This work is supported by the Center for Molecular Magnetic Quantum Materials, an Energy Frontier Research Center funded by the U.S. Department of Energy, Office of Science, Basic Energy Sciences under Award no. DE-SC0019330. Computations were done using the utilities of the University of Florida Research Computing.

## AUTHOR CONTRIBUTIONS

C.J. and S.L. conceived, and C.J. supervised the work. S.L. performed calculations based on the tight-binding model. Y.Z., A.B., and X.Z. performed DFT calculations. S.L. analyzed the data. S.L., Y.Z., X.Z., and C.J. wrote the manuscript, with input from all authors. All authors reviewed the manuscript.

## COMPETING INTERESTS

The authors declare no competing interests.

## ADDITIONAL INFORMATION

**Supplementary Information** The online version contains supplementary material available at ...

**Correspondence** should be addressed to C.J. Request for materials should be directed to S.L..

# Supplementary Materials for “Altermagnetism and Strain Induced Altermagnetic Transition in Cairo Pentagonal Monolayer”

Shuyi Li,<sup>1</sup> Yu Zhang,<sup>1</sup> Adrian Bahri,<sup>1</sup> Xiaoliang Zhang,<sup>1</sup> and Chunjing Jia<sup>1</sup>

<sup>1</sup>Department of Physics, University of Florida, Gainesville, FL 32611, USA

## I. TIGHT-BINDING MODEL

The Cairo pentagonal lattice under consideration is shown in Fig. I. The lattice vectors are defined as  $\mathbf{a}_1 = (a, 0)$  and  $\mathbf{a}_2 = (0, a)$ , where  $a$  is the lattice constant and set to be 1 for convenience. Each primitive unit cell contains two magnetic sites and four non-magnetic sites, their coordinates are

$$\begin{aligned} \text{magnetic} : & (0, 0), \left(\frac{a}{2}, \frac{a}{2}\right) \\ \text{non-magnetic} : & \left(d, \frac{a}{2} - d\right), \left(d - \frac{a}{2}, d\right), \left(-d, d - \frac{a}{2}\right), \left(\frac{a}{2} - d, -d\right), \end{aligned} \quad (\text{S1})$$

where  $0 < d < a/2$ . Without loss of generality, we set spin-up site at  $(0, 0)$ , and  $0 < d = 0.1a < a/4$  in our calculation.

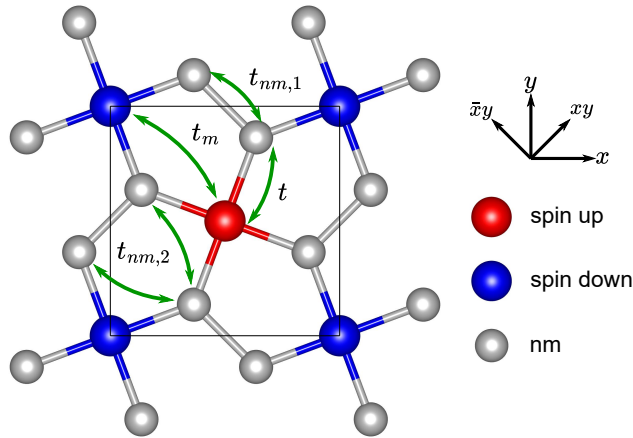


FIG. S1. A schematic of the pentagonal lattice with space group  $P4/mbm$  and the tight-binding model on it.

The tight-binding Hamiltonian is

$$\begin{aligned} H = & -(1 + \delta) \sum_{\langle i,j \rangle_{xy}} t_{ij} c_{i\sigma}^\dagger c_{j\sigma} - (1 - \delta) \sum_{\langle i,j \rangle_{\bar{x}y}} t_{ij} c_{i\sigma}^\dagger c_{j\sigma} - J \sum_{i \in m, \sigma, \sigma'} \mathbf{S}_i \cdot c_{i\sigma}^\dagger \boldsymbol{\sigma}_{\sigma\sigma'} c_{i\sigma'} \\ & + (\epsilon_m - \mu) \sum_{i \in m, \sigma} c_{i\sigma}^\dagger c_{i\sigma} + (\epsilon_{nm} - \mu) \sum_{i \in nm, \sigma} c_{i\sigma}^\dagger c_{i\sigma}, \end{aligned} \quad (\text{S2})$$

where  $\delta$  represents the strength of anisotropy caused by diagonal strains. We perform Fourier transformation into each electron operator

$$c_{i\sigma} = \frac{1}{\sqrt{N}} \sum_{\mathbf{k}} c_{\mathbf{k}\sigma} e^{i\mathbf{r}_i \cdot \mathbf{k}} \quad (\text{S3})$$

, where  $N$  is the number of unit cells. Then the Hamiltonian in Eq. (S2) becomes

$$H = \sum_{\mathbf{k}, \sigma} \psi_{\mathbf{k}\sigma}^\dagger H_{\mathbf{k}\sigma} \psi_{\mathbf{k}\sigma}, \quad (\text{S4})$$

where  $\psi_{\mathbf{k}\sigma}^\dagger = [c_{1\sigma\mathbf{k}}^\dagger, \dots, c_{6\sigma\mathbf{k}}^\dagger]$ . The matrices  $H_{\mathbf{k}\sigma}$  are written as

$$H_{\mathbf{k}\uparrow} = \begin{bmatrix} \epsilon_m - JS & t_{AB} & t_{A\alpha} & t_{A\beta} & t_{A\gamma} & t_{A\eta} \\ t_{AB}^* & \epsilon_m + JS & t_{B\alpha} & t_{B\beta} & t_{B\gamma} & t_{B\eta} \\ t_{A\alpha}^* & t_{B\alpha}^* & \epsilon_{nm} & t_{\alpha\beta} & t_{\alpha\gamma} & t_{\alpha\eta} \\ t_{A\beta}^* & t_{B\beta}^* & t_{\alpha\beta}^* & \epsilon_{nm} & t_{\beta\gamma} & t_{\beta\eta} \\ t_{A\gamma}^* & t_{B\gamma}^* & t_{\alpha\gamma}^* & t_{\beta\gamma}^* & \epsilon_{nm} & t_{\gamma\eta} \\ t_{A\eta}^* & t_{B\eta}^* & t_{\alpha\eta}^* & t_{\beta\eta}^* & t_{\gamma\eta}^* & \epsilon_{nm} \end{bmatrix} - \mu * \mathbb{1}_{6 \times 6}, \quad (\text{S5})$$

and

$$H_{\mathbf{k}\downarrow} = \begin{bmatrix} \epsilon_m + JS & t_{AB} & t_{A\alpha} & t_{A\beta} & t_{A\gamma} & t_{A\eta} \\ t_{AB}^* & \epsilon_m - JS & t_{B\alpha} & t_{B\beta} & t_{B\gamma} & t_{B\eta} \\ t_{A\alpha}^* & t_{B\alpha}^* & \epsilon_{nm} & t_{\alpha\beta} & t_{\alpha\gamma} & t_{\alpha\eta} \\ t_{A\beta}^* & t_{B\beta}^* & t_{\alpha\beta}^* & \epsilon_{nm} & t_{\beta\gamma} & t_{\beta\eta} \\ t_{A\gamma}^* & t_{B\gamma}^* & t_{\alpha\gamma}^* & t_{\beta\gamma}^* & \epsilon_{nm} & t_{\gamma\eta} \\ t_{A\eta}^* & t_{B\eta}^* & t_{\alpha\eta}^* & t_{\beta\eta}^* & t_{\gamma\eta}^* & \epsilon_{nm} \end{bmatrix} - \mu * \mathbb{1}_{6 \times 6}, \quad (\text{S6})$$

where the matrix elements are

$$\begin{aligned} t_{AB} &= -2t_m(1 + \delta) \cos\left(\frac{a}{2}k_x + \frac{a}{2}k_y\right) - 2t_m(1 - \delta) \cos\left(\frac{a}{2}k_x - \frac{a}{2}k_y\right), \\ t_{A\alpha} &= -t(1 - \delta)e^{i\left(\frac{a}{2}-d\right)k_x - dk_y}, \\ t_{A\beta} &= -t(1 - \delta)e^{i\left(-\frac{a}{2}-d\right)k_x + dk_y}, \\ t_{A\gamma} &= -t(1 + \delta)e^{i\left(dk_x + \left(\frac{a}{2}-d\right)k_y\right)}, \\ t_{A\eta} &= -t(1 + \delta)e^{i\left(-dk_x - \left(\frac{a}{2}-d\right)k_y\right)}, \\ t_{B\alpha} &= -t(1 - \delta)e^{i\left(-dk_x + \left(-d + \frac{a}{2}\right)k_y\right)}, \\ t_{B\beta} &= -t(1 - \delta)e^{i\left(dk_x + \left(d - \frac{a}{2}\right)k_y\right)}, \\ t_{B\gamma} &= -t(1 + \delta)e^{i\left(\left(d - \frac{a}{2}\right)k_x - dk_y\right)}, \\ t_{B\eta} &= -t(1 + \delta)e^{i\left(\left(-d + \frac{a}{2}\right)k_x + dk_y\right)}, \\ t_{\alpha\beta} &= -t_{nm,1}(1 + \delta)e^{i(2dk_x + 2dk_y)}, \\ t_{\alpha\gamma} &= -t_{nm,2}(1 + \delta)e^{i\left(\left(2d - \frac{a}{2}\right)k_x - \frac{a}{2}k_y\right)} - t_{nm,2}(1 - \delta)e^{i\left(\left(2d - \frac{a}{2}\right)k_x + \frac{a}{2}k_y\right)}, \\ t_{\alpha\eta} &= -t_{nm,2}(1 + \delta)e^{i\left(-\frac{a}{2}k_x + \left(2d - \frac{a}{2}\right)k_y\right)} - t_{nm,2}(1 - \delta)e^{i\left(\frac{a}{2}k_x + \left(2d - \frac{a}{2}\right)k_y\right)}, \\ t_{\beta\gamma} &= -t_{nm,2}(1 + \delta)e^{i\left(\frac{a}{2}k_x + \left(\frac{a}{2} - 2d\right)k_y\right)} - t_{nm,2}(1 - \delta)e^{i\left(-\frac{a}{2}k_x + \left(\frac{a}{2} - 2d\right)k_y\right)}, \\ t_{\beta\eta} &= -t_{nm,2}(1 + \delta)e^{i\left(\left(\frac{a}{2} - 2d\right)k_x + \frac{a}{2}k_y\right)} - t_{nm,2}(1 - \delta)e^{i\left(\left(\frac{a}{2} - 2d\right)k_x - \frac{a}{2}k_y\right)}, \\ t_{\gamma\eta} &= -t_{nm,1}(1 - \delta)e^{i(-2dk_x + 2dk_y)}, \end{aligned} \quad (\text{S7})$$

and  $\mathbb{1}_{6 \times 6}$  is a  $6 \times 6$  identity matrix.

## II. TAYLOR EXPANSION OF $E_{n,\sigma}(\mathbf{k})$ NEAR $\Gamma$ POINT

We investigate the behavior of band dispersions near  $\Gamma$  point by performing Taylor expansion. Near  $\mathbf{k} = \mathbf{0}$ , we assume that an isolated band can be represented by

$$\begin{aligned} E_\sigma(\mathbf{k}) &= a_{0,\sigma} + a_{21,\sigma}k_x^2 + a_{22,\sigma}k_xk_y + a_{23,\sigma}k_y^2 \\ &+ a_{41,\sigma}k_x^4 + a_{42,\sigma}k_x^3k_y + a_{43,\sigma}k_x^2k_y^2 + a_{44,\sigma}k_xk_y^3 + a_{45,\sigma}k_y^4, \end{aligned} \quad (\text{S8})$$

there is no linear and cubic term because of inversion symmetry. Then we expand the characteristic equation

$$\det|E_\sigma \mathbb{1}_{6 \times 6} - H_{\mathbf{k}\sigma}| = 0 \quad (\text{S9})$$

at  $\mathbf{k} = \mathbf{0}$  to solve the coefficients.

The model parameters used are  $t_m = -0.4$ ,  $t_{nm,1} = 0.9$ ,  $t_{nm,2} = 0.6$ ,  $J = 1$ ,  $\epsilon_m = \epsilon_{nm} = 0$  and  $\mu = 0$ . In the case of  $\delta = 0$ , there are four isolated bands near the  $\Gamma$  point for each spin, the coefficients are in Table. I. The leading term of spin-splitting for the  $n$ th pair bands near the  $\Gamma$  point is

$$\Delta E_n(\mathbf{k}) = 2a_{n,42,\uparrow}k_xk_y(k_x^2 - k_y^2), \quad (\text{S10})$$

which is belong to  $g$ -wave symmetry.

Band Index $n$	1	2	5	6
$a_{0,\uparrow}$	-5.19	0.106	1.5	1.79
$a_{21,\uparrow}$	0.267	-0.414	0.3	0.27
$a_{22,\uparrow}$	0	0	0	0
$a_{23,\uparrow}$	0.267	-0.414	0.3	0.27
$a_{41,\uparrow}$	-0.00425	-0.0341	-0.664	0.0497
$a_{42,\uparrow}$	0.000141	-0.166	1.35	-0.491
$a_{43,\uparrow}$	-0.0111	0.631	-0.551	-0.00221
$a_{44,\uparrow}$	-0.000141	0.166	-1.35	0.491
$a_{45,\uparrow}$	-0.00425	-0.0341	-0.664	0.0497
$a_{0,\downarrow}$	-5.19	0.106	1.5	1.79
$a_{21,\downarrow}$	0.267	-0.414	0.3	0.27
$a_{22,\downarrow}$	0	0	0	0
$a_{23,\downarrow}$	0.267	-0.414	0.3	0.27
$a_{41,\downarrow}$	-0.00425	-0.0341	-0.664	0.0497
$a_{42,\downarrow}$	-0.000141	0.166	-1.35	0.491
$a_{43,\downarrow}$	-0.0111	0.631	-0.551	-0.00221
$a_{44,\downarrow}$	0.000141	-0.166	1.35	-0.491
$a_{45,\downarrow}$	-0.00425	-0.0341	-0.664	0.0497

TABLE I. Coefficients of  $E_{n,\sigma}(\mathbf{k})$  in the case of  $\delta = 0$ .

Band Index $n$	1	2	3	4	5	6
$a_{0,\uparrow}$	-0.519	0.0821	0.81	0.99	1.4	1.91
$a_{21,\uparrow}$	0.266	-0.416	-0.228	-0.0392	0.0625	0.355
$a_{22,\uparrow}$	0.0401	-0.203	0.432	-0.804	0.756	-0.221
$a_{23,\uparrow}$	0.268	-0.392	-0.0054	-0.894	1.01	0.0129
$a_{0,\downarrow}$	-0.519	0.0821	0.81	0.99	1.4	1.91
$a_{21,\downarrow}$	0.268	-0.392	-0.0054	-0.894	1.01	0.0129
$a_{22,\downarrow}$	0.0401	-0.203	0.432	-0.804	0.756	-0.221
$a_{23,\downarrow}$	0.266	-0.416	-0.228	-0.0392	0.0625	0.355

TABLE II. Coefficients of  $E_{n,\sigma}(\mathbf{k})$  in the case of  $\delta = 0.1$ .

In the case of  $\delta = 0.1$ , there are six isolated bands near the  $\Gamma$  point for each spin, the coefficients are in Table. II. The leading term of spin-splitting for the  $n$ th pair bands near the  $\Gamma$  point is

$$\Delta E_n(\mathbf{k}) = (a_{n,21,\uparrow} - a_{n,23,\uparrow})(k_x^2 - k_y^2), \quad (\text{S11})$$

which is belong to  $d$ -wave symmetry.

### III. BAND DEGENERACY UNDER $t_{nm,1} = 0$ AND $t_{nm,2} = 0$

The case of  $t_{nm,1} = 0$  is equivalent to that of a lattice with  $d = a/4$ , which is shown in Fig. S2. This system clearly exhibits mirror symmetries  $\mathcal{M}_x$  and  $\mathcal{M}_y$ .

The case of  $t_{nm,2} = 0$  is equivalent to that of a lattice with  $d = 0$ . With this formula, it can be directly shown that the characteristic equations of  $H_{kx,ky,\sigma}$ ,  $H_{kx,-ky,\sigma}$ , and  $H_{-kx,ky,\sigma}$  are the same:

$$\begin{aligned} \det|E\mathbb{1}_{6\times 6} - H_{kx,ky,\sigma}| &= \det|E\mathbb{1}_{6\times 6} - H_{kx,-ky,\sigma}|, \\ \det|E\mathbb{1}_{6\times 6} - H_{kx,ky,\sigma}| &= \det|E\mathbb{1}_{6\times 6} - H_{-kx,ky,\sigma}|, \end{aligned} \quad (\text{S12})$$

which implies that  $E_{n,\sigma}(kx,ky) = E_{n,\sigma}(kx,-ky) = E_{n,\sigma}(-kx,ky)$ . The combination of these symmetries with  $\{C_{2\perp}||\mathcal{M}_x\}$  and  $\{C_{2\perp}||\mathcal{M}_y\}$  ensures that  $E_{n,\uparrow}(\mathbf{k}) = E_{n,\downarrow}(\mathbf{k})$ .

### IV. BERRY CURVATURE

After taking into account the symmetry breaking terms

$$H_1 = \sum_{i \in (m\uparrow), \sigma} \sum_{\xi} (t_1 c_{i,\sigma}^\dagger c_{i+\xi\sigma} - t_1 c_{i\sigma}^\dagger c_{i-\xi,\sigma}) + h.c. \quad (\text{S13})$$

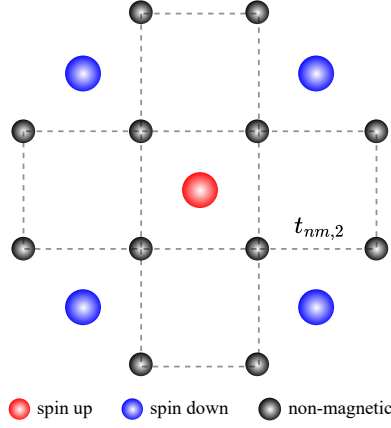


FIG. S2. The equivalent lattice of the Cairo pentagonal lattice when  $t_{nm,1} = 0$  in its tight-binding model.

and

$$H_2 = - \sum_{i \in (m\uparrow), \sigma} (-1)^\sigma \sum_{\xi} i(t_2 c_{i,\sigma}^\dagger c_{i+\xi,\sigma} + t_2 c_{i,\sigma}^\dagger c_{i-\xi,\sigma}) + h.c., \quad (\text{S14})$$

we perform the same process as in Eq.(S3) and Eq.(S4) to obtain the Hamiltonian matrix  $H_{\mathbf{k}\sigma}^{total}$ . Then we use Fukui's method to calculate Berry curvature  $\Omega_{n,\sigma}(\mathbf{k})$  and Chern number  $\mathcal{C}_{n,\sigma}$  numerically [S1], which is given by

$$\begin{aligned} & \Omega_{n,\sigma}(k_x + \frac{1}{2}\delta k_x, k_y + \frac{1}{2}\delta k_y) \\ &= - \frac{1}{\delta k_x \delta k_y} \text{Arg}[\langle u_{n,\sigma}(k_x, k_y) | u_{n,\sigma}(k_x + \frac{1}{2}\delta k_x, k_y) \rangle \\ & \langle u_{n,\sigma}(k_x + \frac{1}{2}\delta k_x, k_y) | u_{n,\sigma}(k_x + \frac{1}{2}\delta k_x, k_y + \frac{1}{2}\delta k_y) \rangle \\ & \langle u_{n,\sigma}(k_x + \frac{1}{2}\delta k_x, k_y + \frac{1}{2}\delta k_y) | u_{n,\sigma}(k_x, k_y + \frac{1}{2}\delta k_y) \rangle \\ & \langle u_{n,\sigma}(k_x, k_y + \frac{1}{2}\delta k_y) | u_{n,\sigma}(k_x, k_y) \rangle], \end{aligned} \quad (\text{S15})$$

$$\mathcal{C}_{n,\sigma} = \frac{1}{2\pi} \sum_{\mathbf{k}} \Omega_{n,\sigma}(k_x + \frac{1}{2}\delta k_x, k_y + \frac{1}{2}\delta k_y) \delta k_x \delta k_y, \quad (\text{S16})$$

where  $|u_{n,\sigma}(k_x, k_y)\rangle$  is the  $n$ th eigenvector of the Hamiltonian  $H_{\mathbf{k}\sigma}^{total}$ . In the summation, we choose  $\delta k_x = \delta k_y = 2\pi/N_s$  with  $N_s = 201$ .

## V. DETAILS OF AB INITIO CALCULATIONS

We use the Vienna Ab initio Simulation Package (VASP) [S2] for all density-functional theory calculations. Projector-augmented-wave (PAW) potentials [S3] were utilized for ion-electron interactions, and the generalized gradient approximation (GGA) with the Perdew-Burke-Ernzerhof (PBE) functional [S4] was applied to describe electron exchange-correlation interactions. The energy cutoff was set to 600 eV.

In the calculation of FeS<sub>2</sub>, a  $15 \times 15 \times 1$  Monkhorst-Pack  $k$  point mesh was used and the GGA + U approach was adopted with  $U_{eff} = 2.0$  eV [S5]. The monolayer FeS<sub>2</sub> is exfoliated from the bulk crystal in the (100) plane, forming a planar structure by manually relocating the S atoms. In our calculations, spin-orbit coupling is not included, resulting in the absence of magnetic anisotropy. To determine the magnetic ground state, we relaxed the structure under the ferromagnetic (FM) and Néel antiferromagnetic (AFM) configurations with 0.015 eV/Å and  $10^{-6}$  eV as the convergence criterion for residual force and total-energy, respectively:

$$E_{FM} = -29.138344 \text{ eV}, \quad E_{AFM} = -30.641527 \text{ eV}. \quad (\text{S17})$$

The results suggest that the Néel antiferromagnetic configuration has a lower energy with  $\Delta E = -1.50$  eV. Keeping the lengths of lattice vectors unchanged, we apply shear strain in the diagonal direction by changing the angle  $\gamma$  between lattice vectors  $\mathbf{a}$  and  $\mathbf{b}$  from  $90^\circ$  to  $88^\circ$  and relax the atomic positions.

For Nb<sub>2</sub>FeB<sub>2</sub>, a  $8 \times 8 \times 13$  Monkhorst-Pack  $k$ -point mesh was used, and  $U_{eff} = 4.82$  eV [S6] was set for strongly correlated Fe 3d electrons. We relax both lattice constant and atomic positions until the atomic force is less than

0.01eV/Å.

---

- [S1] T. Fukui, Y. Hatsugai, and H. Suzuki, Chern numbers in discretized brillouin zone: efficient method of computing (spin) hall conductances, *Journal of the Physical Society of Japan* **74**, 1674 (2005).
- [S2] G. Kresse and J. Hafner, Ab initio molecular-dynamics simulation of the liquid-metal–amorphous-semiconductor transition in germanium, *Phys. Rev. B* **49**, 14251 (1994).
- [S3] P. E. Blöchl, Projector augmented-wave method, *Phys. Rev. B* **50**, 17953 (1994).
- [S4] J. P. Perdew, K. Burke, and M. Ernzerhof, Generalized gradient approximation made simple, *Phys. Rev. Lett.* **77**, 3865 (1996).
- [S5] A. B. Puthirath, A. P. Balan, E. F. Oliveira, V. Sreepal, F. C. Robles Hernandez, G. Gao, N. Chakingal, L. M. Sassi, P. Thibeorchews, G. Costin, R. Vajtai, D. S. Galvao, R. R. Nair, and P. M. Ajayan, Apparent ferromagnetism in exfoliated ultrathin pyrite sheets, *The Journal of Physical Chemistry C* **125**, 18927 (2021).
- [S6] Z.-F. Gao, S. Qu, B. Zeng, Y. Liu, J.-R. Wen, H. Sun, P.-J. Guo, and Z.-Y. Lu, Ai-accelerated discovery of altermagnetic materials, arXiv preprint arXiv:2311.04418 (2023).